ARTICLE

Isolation and Characterization of Few-Layer Manganese Thiophosphite

Gen Long,[†][ID] Ting Zhang,[†,‡] Xiangbin Cai,[†] Jin Hu,[§,⊥] Chang-woo Cho,[†] Shuigang Xu,[†,∥] Junying Shen,[†] Zefei Wu,[†] Tianyi Han,[†] Jiangxiazi Lin,[†] Jingwei Wang,[†] Yuan Cai,[†] Rolf Lortz,[†] Zhiqiang Mao,[§] and Ning Wang*,[†][ID]

[†]Department of Physics and Center for Quantum Materials and [‡]Institute for Advanced Study, The Hong Kong University of Science and Technology, Hong Kong, China
[§]Department of Physics and Engineering Physics, Tulane University, New Orleans, Louisiana 70118, United States
[∥]National Graphene Institute, University of Manchester, Manchester M139PL, United Kingdom

[S] *Supporting Information*

ABSTRACT: This work reports an experimental study on an antiferromagnetic honeycomb lattice of $MnPS_3$ that couples the valley degree of freedom to a macroscopic antiferromagnetic order. The crystal structure of $MnPS_3$ is identified by high-resolution scanning transmission electron microscopy. Layer-dependent angle-resolved polarized Raman fingerprints of the $MnPS_3$ crystal are obtained, and the Raman peak at 383 cm^{-1} exhibits 100% polarity. Temperature dependences of anisotropic magnetic susceptibility of the $MnPS_3$ crystal are measured in a superconducting quantum interference device. Anisotropic behaviors of the magnetic moment are explored on the basis of the mean field approximation model. Ambipolar electronic conducting channels in $MnPS_3$ are realized by the liquid gating technique. The conducting channel of $MnPS_3$ offers a platform for exploring the spin/valleytronics and magnetic orders in 2D limitation.

KEYWORDS: $MnPS_3$, Raman spectroscopy, antiferromagnetic, magnetic susceptibility, electronic transport
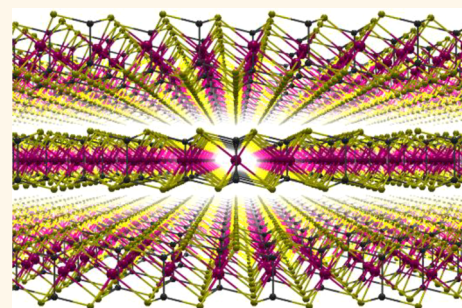
The magnetic order in 2D limitation is of boundless interest not only for fundamental condensed matter studies but also as a potential candidate in numerous technological applications.[1−7] Despite the extensive family of 2D crystals, only a few exhibit intrinsic magnetic orders.[8,9] Therefore, research has been mostly limited to the magnetic orders arising from extrinsic effects, such as vacancies, defects, edges, or chemical dopants.[10−15] An emerging 2D crystal group, namely, transition-metal thiophosphite (TMT) (MPX3; M = Fe, Ni, Mn, Cd, Zn, *etc.*; P = P; X = S, Se, *etc.*), offers possibilities because of the suitability of TMT as a platform for exploring intrinsic magnetic orders.[16−18] Different transition-metal ions in TMT accumulate different antiferromagnetic orders. $FePS_3$ is best described by the Ising model and $MnPS_3$ by the isotropic Heisenberg model.[5,16] The intrinsic degrees of electronic freedom, such as charge and spin, have been broadly explored in the last few decades in electronics and spintronics.[19−22] In recent years, an electron valley freedom has drawn much attention because of its immense potential for fundamental studies on quantum concepts and next-generation electronics.[23−25] This valley freedom is predicted to couple with antiferromagnetic order in $MnPS_3$ because of the latter's antiferromagnetic honeycomb lattice.[26] Coupling the micronature to the macrophenomena renders $MnPS_3$ an ideal playground for exploring electronic degrees of freedom. In this work, we perform a systematic optical and electronic transport study of $MnPS_3$ in an atomically thin level. In addition to identifying the crystal structure with high-resolution scanning transmission electron microscopy (HRSTEM), Raman fingerprints of $MnPS_3$ with different thicknesses are also determined through angle-resolved polarized Raman (ARPR) spectroscopy. Temperature dependence of magnetic susceptibility of $MnPS_3$ is measured by a superconducting quantum interference (SQUID) magnetometer. Anisotropic behaviors of magnetic moment are studied based on the mean field approximation (MFA) model. Last, we develop a liquid gating (LG) technique and fabricate $MnPS_3$-based electrical double-layer transistors (EDLTs) to determine its electronic transport properties. Benefiting from the high efficiency of LG,[27] an ambipolar conducting channel is observed with thickness-dependent carrier mobility of a few $cm^2\ V^{-1}\ s^{-1}$ in $MnPS_3$.

RESULTS AND DISCUSSION

Top view of monolayer $MnPS_3$ is illustrated in Figure 1a (top-left panel). Each $[P_2S_6]^{4-}$ unit is located at the center of a
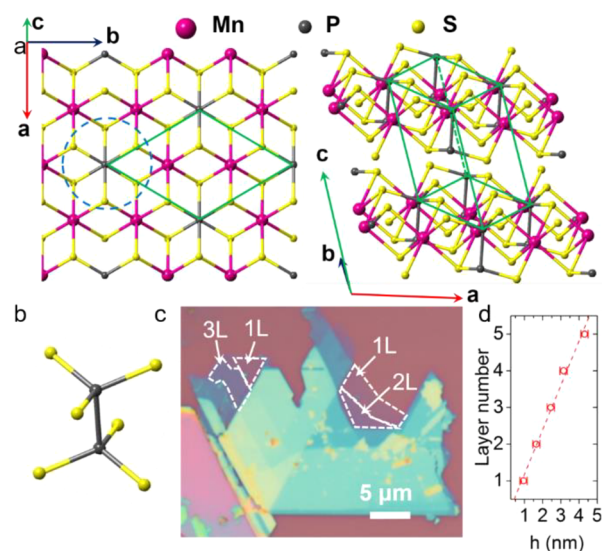

Figure 1. Crystal structure of $MnPS_3$. (a) Ball-and-stick model of the $MnPS_3$ crystal structure. The left panel shows the top view of the monolayer model. The green parallelogram indicates the primary unit cell. The arrows show the crystalline orientations (red, *a*; blue, *b*; greed, *c*). The right panel displays the side view of the bilayer model, and the green parallelepiped indicates the primary unit cell of the $MnPS_3$ bulk crystal. (b) Dumbbell-shaped structure of the $[P_2S_6]^{4-}$ unit is marked by the dashed light blue circle in (a). (c) Micro-optical image of an exfoliated few-layer $MnPS_3$. The scale bar denotes 5 μm. (d) Measured thicknesses *h* and corresponding layer numbers. The red dashed line represents the linear fitting result.

regular hexagon with six corners occupied by $[Mn]^{2+}$. The dumbbell-shaped structure of $[P_2S_6]^{4-}$ is shown in Figure 1b. All the $[Mn]^{2+}$ are arranged in a honeycomb structure, and each $[Mn]^{2+}$ is surrounded by six sulfur atoms. The zigzag direction of $[Mn]^{2+}$ is defined as the *a* direction, whereas the armchair direction (perpendicular to *a*) is defined as *b*. The point group of monolayer $MnPS_3$ is assigned to be $\overline{3}2/m$.[28] The three-fold inverse rotation symmetry results in a valley degeneracy at the corner (K point) of the hexagonal first Brillouin zone (BZ). When stacked together along the *c* direction ($\beta = 107.5°$), the atomic layers break the three-fold inverse rotation symmetry and render the bulk $MnPS_3$ a monoclinic structure with a point group of $2/m$ (Figure 1a, right panel). We notice that single molecular layers of $Mn_{0.8}PS_3$ and $Cd_{0.8}PS_3$ in suspension in water have been obtained by the ion exchange method.[29] However, the ion exchange leads to structure factor modulations and prohibits access to the intrinsic properties of a few-layer $MnPS_3$ crystal.[29] Given the weak van der Waals interaction between atomic layers, the mono- and few-layered $MnPS_3$ flakes can be mechanically exfoliated from the bulk crystal by the scotch tape method.[30,31] Figure 1c shows a representative micro-optical image of $MnPS_3$, with different layers showing distinct optical contrasts due to light interference. To confirm the thicknesses of these flakes, we perform atomic force microscopy (AFM) measurement, and a thickness *h* of 0.8 nm is obtained for one atomic layer (Figure 1d), which agrees well with the layer space of 0.65 nm.[32]

While exfoliating the bulk crystal, we find that most (>90%) of the flakes exhibit hexagonal shapes with inner angles of ~120° or 60° (Figure 1c). To elucidate the mechanism behind the special angles, we compare between the selected area electron diffraction (SAED) pattern and its defocused trans-mitted spot to index the edges of the exfoliated $MnPS_3$ flakes. The $MnPS_3$ flake is kept fixed along the *c* direction (Figure 2a), and the focus is adjusted until the real space features are visible
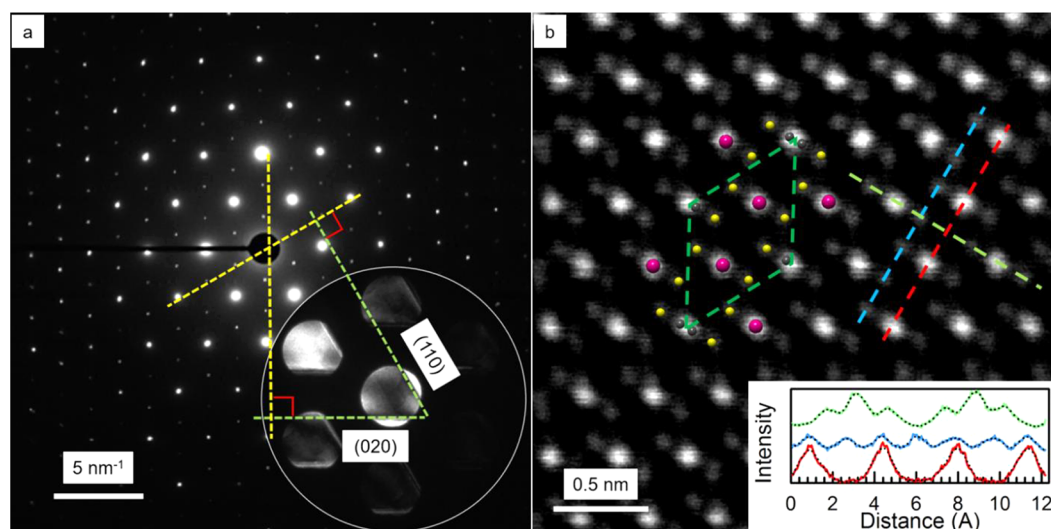

Figure 2. Transmission electron microscopy images of $MnPS_3$. (a) SAED pattern of $MnPS_3$. The scale bar represents 5 nm^{-1}. The inset shows the defocused diffraction pattern at the same site. The real space features are apparent in the defocused transmitted spot. The light green dashed lines indicate the two edges of the $MnPS_3$ sample, whereas the yellow dashed lines show the directions perpendicular to the two edges. A magnetic declination of 3° is corrected. The two edges are indexed to be (110) and (020) according to the diffraction patterns. (b) HAADF STEM image of $MnPS_3$ sample along *c* direction. The scale bar represents 0.5 nm. The colored balls indicate the different elements in the image (purple, Mn; black, P; yellow, S). The dashed green parallelogram denotes the primary unit cell. The inset indicates that the intensities vary with distance along the directions, as marked by the dashed lines with the same colors. A constant offset between different lines is introduced for a clear display.

inside the transmitted spot (Figure 2a, inset). The two edges forming a 60° angle are indexed to be (110) and (020) according to the perpendicular relation between the reciprocal space and real space. The (110) and (020) directions correspond to the zigzag directions of $[Mn]^{2+}$ in the $MnPS_3$ structure. This result can be readily explained by the weakest breaking strength along the zigzag direction of $[Mn]^{2+}$.[33] To verify this conclusion, we obtain a high-angle annular dark-field (HAADF) HRSTEM image of the same sample along the c direction (Figure 2b). Each bright spot corresponds to a single atom; the three elements are indicated by different colored balls, and primary unit cell is marked by a green-dashed parallelogram. The six-membered ring composed of manganese atoms is clearly visible. The variation in intensity along the dashed lines are displayed in the right bottom inset. The lattice parameters extracted from the image ($a = 6.08 \pm 0.05$ nm; $b = 10.52 \pm 0.05$ nm) agree with the values measured from neutron scattering experiment[32] and those obtained from X-ray analysis.[28]

Besides structural identification, we also examine the Raman fingerprints of $MnPS_3$ with different layer numbers. Figure 3a
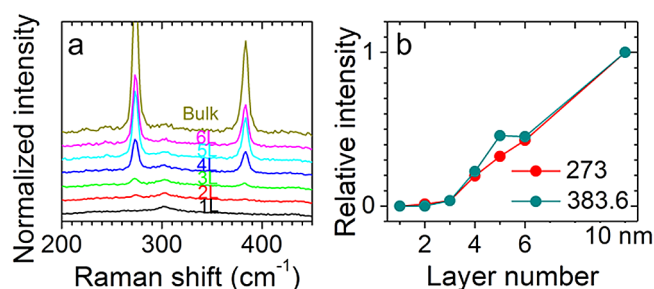

Figure 3. Thickness-dependent Raman spectrum of $MnPS_3$. (a) Raman spectra of $MnPS_3$ with different thicknesses (monolayer to 10 nm (~12 layers)). The Raman intensities are normalized to the Raman peak intensity of substrate Si near 520 cm^{-1}. (b) $MnPS_3$ Raman peak intensities change with thickness. The peak intensities of the 10 nm sample is regarded as one unit.

shows the Raman spectra of $MnPS_3$ with different layers collected at room temperature. Two Raman peaks are apparent (P_{273}, 273 cm^{-1}; P_{383}, 383.6 cm^{-1}; the Raman peak at 302 cm^{-1} is the second-order Raman peak of silicon substrate[34]) in the 10 nm samples. The intensities of P_{273} and P_{383} decrease dramatically with decreasing layer number and disappear in

the monolayer flake (Figure 3b). The main Raman spectral features for the monolayer, bilayer, and trilayer flakes are summarized below. Monolayer flakes exhibit no observable Raman peaks. When layer number increases to two, both P_{273} and P_{383} emerge, and P_{383} is considerably weaker than P_{273}. For three-layer flakes, the two peaks at 273 and 383 cm^{-1} exhibit similar intensities. The clear dependence of Raman peak intensities on layer number renders the Raman spectrum a reliable criterion for determining the thickness of a few-layer $MnPS_3$ sample.

To probe further into symmetry properties, we perform ARPR spectral measurements on a four-layer $MnPS_3$ flake at room temperature. The ARPR measurement configuration is shown in the top-right inset of Figure 4a. The a direction (green arrow) runs along one of the edges of the exfoliated $MnPS_3$ flakes (zigzag direction of $MnPS_3$), and the b direction (blue arrow) is perpendicular to a direction. The linear polarization direction of the incident laser (purple arrow), and scattered light (light blue arrow) was illustrated, as well. The definitions of angles α and θ are shown in the inset. Figure 4a presents the ARPR spectra varying with α when θ is fixed at 0°. P_{273} remains unchanged with increasing α, whereas the peak at 383 cm^{-1} varies periodically with α. Moreover, P_{383} reaches its maximum at 0 and 180° and disappears at around 90°. This pattern demonstrates a 100% polarity of the Raman peak at 383 cm^{-1}.[35,36] We perform a fine α (every 10°)-dependent ARPR measurement, and the extracted intensities of the two peaks are shown in Figure 4b. The black solid line implies $I(\alpha) = I(\alpha = 0) \times \cos^2(\alpha)$, as expected and measured in varying systems. By contrast, the red dashed line confirms the depolarized feature of P_{273}.[36] The polarized and depolarized behaviors of Raman peaks demonstrate different symmetry properties of the corresponding phonon modes. Specifically, the polarized behavior of the Raman peak signifies that the peaks arise from totally symmetric variations. Figure 4c presents the observed ARPR spectra at a few different θ with α fixed at 0°. The independence of the ARPR spectrum on θ demonstrates that the crystalline orientation hardly affects the Raman spectrum of $MnPS_3$. The same anisotropic behaviors of the two Raman peaks are also observed in a 10 nm thick $MnPS_3$ flake (Supporting Information). The phonon spectrum and corresponding Raman susceptibilities at the center of the first BZ are calculated through the density function perturbation theory (DFPT)[37−40] to assign the Raman modes and phonon frequencies (Supporting Information). The bulk crystal of
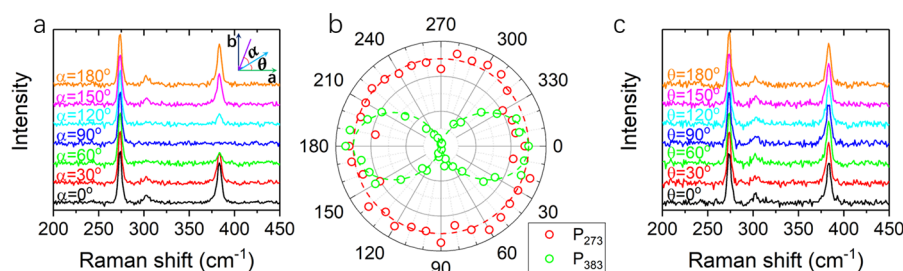

Figure 4. Angle-resolved polarized Raman spectrum of four-layer $MnPS_3$. (a) Polarized Raman spectra of $MnPS_3$ with $\theta = 0$. The top-right inset shows the ARPR spectrum measurement configuration. The green and blue arrows indicate the a and b directions, respectively. The purple and light blue arrows indicate the linear polarization directions of the incident and scattered lights, respectively. Angle α is the angle between the incident and scattered lights, whereas angle θ is the angle between the scattered light and the a direction. (b) α-Dependent polarized Raman peak intensities with $\theta = 0$ (red, P_{283}; green, P_{383}). The peak intensities at $\alpha = 0$ are considered as one unit. The red and green dashed lines display the fitting results of constant intensity and $\cos^2(\alpha)$, respectively. (c) θ-Dependent polarized Raman spectrum with $\alpha = 0$.
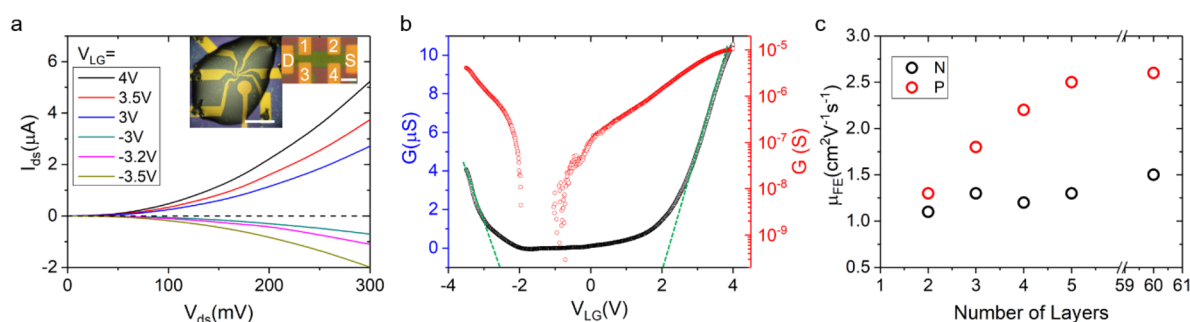
Figure 5. Transport features of electrical double-layer transistor based on MnPS$_3$. (a) Output curves of MnPS$_3$ at different LG voltages. Current of electrons (positive LG voltage) are shown with positive indices, and those of holes (negative LG voltage) are shown with negative indices. The two insets show the micro-optical images of an EDLT in different ratios. The scale bars denote 300 μm (left) and 3 μm (right). (b) Room temperature transfer characteristics in linear (black dots) and log (red dots) scales of the MnPS$_3$ EDLT. The green dashed lines show the linear fitting result of transfer characteristics. (c) Field effect mobilities of holes (red) and electrons (black) of MnPS$_3$ flakes with thicknesses ranging from two layers to around 60 layers.

MnPS$_3$ belongs to the $C2/m$ symmetry group. The 30 irreducible phonon modes at the first BZ center are expressed as $\Gamma = 8A_g + 6A_u + 7B_g + 9B_u$ and confirmed by the calculation results. Our calculation result agrees well with the reported one.[41] Polarized peak at 383 cm^{-1} is assigned to the A$_g$ mode, whereas the depolarized peak at 273 cm^{-1} is assigned to the B$_g$ mode according to the symmetry elements of the A$_g$ and B$_g$ modes.[41,42]

The electronic transport properties of MnPS$_3$ flakes with thickness ranging from two layers to 60 layers (around 50 nm) are probed. A large MnPS$_3$ band gap of more than 3 eV disables chemical potential tuning between the conduction and valence bands by using a field effect with SiO$_2$ or boron nitride as a dielectric layer.[3] Hence, an LG technique is applied to fabricate the EDLTs, which exhibit increased efficiency (about 2 orders of magnitude) in tuning the carrier density with respect to that of 300 nm thick SiO$_2$.[27] The high efficiency of LG enables the observation of an ambipolar conducting channel in MnPS$_3$. The two-terminal output curves (Figure 5a) of a MnPS$_3$ EDLT device of two-layer channel thickness show large current modulations by both positive and negative LG voltages V_{LG}. The channel current I_{ds} exhibits super-linear dependences on the excitation voltage V_{ds}, which is likely caused by a large contact resistance. The improved contact quality therefore enhances the device performance. The top-left inset shows the optical image of a typical EDLT device, and the top-right inset presents the magnified image of the same device. Figure 5b reveals the transfer curve, and the dramatic increase in channel conductance G when V_{LG} is higher (lower) than the positive (negative) threshold voltage demonstrates the ambipolar conducting operation of our EDLTs. When V_{LG} varies from +4 to −3.5 V, the channel switches from n-type "on" state to "off" state and changed to p-type "on" state with an on/off ratio more than 10^4. The on/off ratio is comparable with the values in widely studied TMDCs. The "off" state roughly ranges from V_{LG} = −2.7 V to V_{LG} = 2.2 V, resulting in a "gap" of 4.9 V, and this value of 4.9 V is consistent with the calculated band gap of MnPS$_3$ crystal.[4,43,44] The field effect carrier mobility $\mu = \frac{1}{C}\frac{dG}{dV_{LG}}\frac{L}{W}$, where C = 8.4 μF cm^{-2} is the equivalent capacitance of LG,[27] and L and W are the length and width of the conducting channel, respectively, estimated for both electrons and holes. The mobility values for electrons and holes are obtained to be ∼1.1 and ∼1.3 cm^2 V^{-1} s^{-1}, respectively. Besides the measurements of bilayer MnPS$_3$

flakes, we obtain the flake thickness dependence of electronic transport behaviors (Supporting Information). In Figure 5c, we plot the charge carrier mobilities as a function of flake thickness. The electron mobility is rather weakly dependent on flake thickness, which can be ascribed to a combination of three factors. First, the induced charge carriers are confined on the first one or two layers of MnPS$_3$ flakes due to the static screening effect. The confinement effect has been reported in different layered materials,[27,45] and the confined charge carrier distribution is independent of the flake thickness. Second, the flake thickness barely exhibits an impact on the conduction band of MnPS$_3$ flakes as predicted by theoretical literature.[43,44] Third, the 3D MnPS$_3$ bulk has been demonstrated as a high resistor that exhibits a high resistivity of 10^{13} Ωcm.[46,47] The intrinsic layers below the biased ones contribute no parallel conducting channels to prohibit the access to the intrinsic properties to the biased one or two layers. As a contrast, the charge mobility of holes gradually increases when the MnPS$_3$ flake becomes thicker and thicker and finally saturates when the flake is thicker than five layers. The saturated mobility is roughly twice that of bilayer flakes. The saturating behavior of hole mobility for a flake thicker than five layers arises from the similar sources with the thickness-independent electron mobility. When flake is thinner than five layers, the thickness dependence of hole mobility may indicate that the magnetic orders in MnPS$_3$ are modified by the thickness. First, the highest valence band is occupied by the 3d^5 electrons of [Mn]$^{2+}$, which construct the magnetic moment of the MnPS$_3$ crystal.[26,43,44] The same electrons also carry the channel current of p-type MnPS$_3$ conducting channels. Hence, the change of charge carrier mobility of p-type channels indicates the modification of magnetic orders in the MnPS$_3$ crystal thinner than five layers. More theoretical and experimental studies are needed to address the complicated dependences of carrier mobility, magnetic orders, and flake thicknesses. 2D MnPS$_3$ flakes are interesting material because their properties can be modified *in situ* by applying V_{LG}. It is noticeable that the efficiency of our LG to modify the conductance of 2D MnPS$_3$ flakes (on/off ratio = 10^4) is 10^3 higher than that of light illustrating on 3D MnPS$_3$ bulks (photo/dark ratio <10).[46,48] The ambipolar performance, as well as the high on/off ratio, renders MnPS$_3$ a promising material for low-energy consuming devices with complementary logic. These desirable attributes are crucial to a superb noise margin and robust operation. The creation of an ambipolar conducting channel opens an avenue

for exploring the magnetic order in 2D antiferromagnetic systems. This channel also supplies an ideal terrace for probing valleytronics coupled to antiferromagnetic orders.

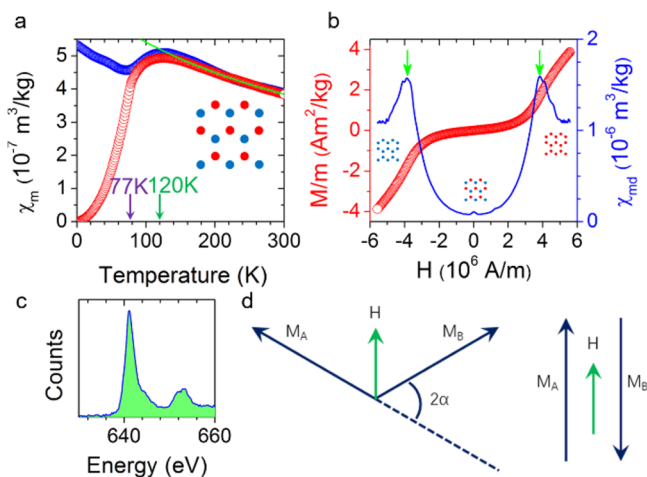Figure 6a reveals the temperature dependences of mass magnetic susceptibilities χ_m of MnPS$_3$ bulk crystal for two

Figure 6. Magnetic susceptibility of MnPS$_3$. (a) Temperature dependences of mass magnetic susceptibility χ_m with in-plane (blue) and out-of-plane (red) magnetic fields of 1600 A/m. The green line shows the fitting result of Curie−Weiss formula. The purple arrow indicates the critical temperature between paramagnetic and antiferromagnetic orders. The green arrow indicates the temperature corresponding to the peak value of χ_m. The inset displays the magnetic order of MnPS$_3$ in antiferromagnetic order regime (blue, spin-up; red, spin-down; or inverse). (b) Mass magnetization (red) and derivative mass susceptibility (blue) as functions of out-of-plane magnetic field at T = 5 K. The three inset patterns display the magnetic orders at magnetic field ranges (blue, spin-up; red, spin-down; or inverse). The green arrows indicate the peak positions of derivative mass susceptibility. (c) EELS of the few-layer sample shows characteristic peaks from [Mn]$^{2+}$. (d) Mean field approximation model for in-plane (left) and out-of-plane (right) field magnetic susceptibility in antiferromagnetic regime. M_A and M_B indicate the magnetizations with opposite orientations; H is the applied magnetic field.

directions, in-plane $\chi_{m//}$ and out-of-plane $\chi_{m\perp}$ magnetic fields, measured in the SQUID magnetometer. When the temperature is above 200 K, the isotropic $\chi_{m//}$ and $\chi_{m\perp}$ demonstrate a Heisenberg-type magnetic order in MnPS$_3$.[49] In the high-temperature paramagnetic phase, χ_m follows the Curie−Weiss law $\chi_m = C/(T - T_C)$, where $C = (2.65 \pm 0.05) \times 10^{-4}$ m^3 K kg^{-1} is the Curie constant and $T_C = -390$ K is the Curie temperature. According to the MFA model when temperature is sufficiently high, the effective magnetic moment μ_{eff} of [Mn]$^{2+}$ could be extracted from the Curie constant according to $C = \frac{2\mu_0 N\mu_{eff}^2}{3k_B}$, where μ_0 is the vacuum permeability, N is the primitive unit cell number per unit mass (also the number of [Mn]$^{2+}$ pairs per unit mass), and k_B denotes the Boltzmann constant.[50,51] The derived μ_{eff} = 5.6 μ_B agrees well with the total magnetic moment of 3d^5 electron system in high spin state (S = 5/2) μ_{3d^5} = 5.9 μ_B.[16] To confirm the obtained electronic state of Mn element in the MnPS$_3$ crystal, we performed the electron energy loss spectroscopy (EELS) of few-layer flakes (Figure 6c). The Mn-L$_{2,3}$ edge energy loss near-edge structures and the chemical shift agree well with the reported [Mn]$^{2+}$ spectrum.[52] The value of μ_{eff} demonstrates that manganese is in the form of

ions rather than atomic form in MnPS$_3$. An large hump at 120 K can be described by the critical fluctuation model.[9,53] As temperature cools, the Curie−Weiss law fails to describe the behavior of χ_m. Further cooling the sample, $\chi_{m\perp}$ sharply decreases to 0, while $\chi_{m//}$ remains essentially constant, signaling the antiferromagnetic order in MnPS$_3$ with T_N = 77K. T_N is consistent with the report value of 78 K.[49]

The contrasting behaviors between $\chi_{m\perp}$ and $\chi_{m//}$ in the low-temperature regime agree well with the MFA model. The left (right) panel of Figure 6d presents the magnetic susceptibility measurement configuration with an applied magnetic field H perpendicular (parallel) to the spin orientations. When H is perpendicular to the spin orientations, the system energy density can be expressed as $U = -\mu_0\lambda M^2(1 - 0.5(2\alpha^2)) - 2\mu_0^2 HM\alpha$, where λ is the Weiss constant, $M = |M_A| = |M_B|$ is the magnetization strength for the [Mn]$^{2+}$ with unit orientation, α is the orientation of M_A and M_B caused by H. U reaches its minima at $\alpha = \mu_0 H/2\lambda M$, hence the magnetic susceptibility with H perpendicular to spin orientations (in-plane magnetic field) $\chi_{//} = \frac{2M\alpha}{H} = \frac{\mu_0}{\lambda}$ is a constant. The observed slight increase of $\chi_{m//}$ when cooling (Figure 6a) signals the onset of long-ranged antiferromagnetic order arising from a combination of dipole−dipole anisotropy with interplanar coupling when temperature is lower than T_N.[18,32,53,54] When H is normal to the layers (right panel of Figure 6d), M_A and M_B make equal angles with H and the magnetic field is not changed, and the $\chi_\perp(T = 0) = 0$, which agrees well with the measured results. Figure 6b presents the mass magnetization accompanied by the derivative mass magnetic susceptibility defined as $\chi_{md} = \frac{1}{m}\frac{dM}{dH}$ with magnetic field perpendicular to the layer plane at T = 5 K. The mass magnetization exhibits a spin-flop transition feature at $H_C = 3.8 \times 10^6$ A/m corresponding to the peak of χ_{md},[55,56] as illustrated by the three insets. It is worth noting that the exchange energies of [Mn]$^{2+}$ have been accurately measured using the neutron scattering technique.[57]

CONCLUSIONS

In summary, a few-layer MnPS$_3$ crystal offers a productive platform for exploring antiferromagnetic order and valley degrees of electron freedom in 2D limitation. Fundamental crystal parameters, such as lattice constants, layer-dependent Raman fingerprints, and Raman peak anisotropy are measured by HRSTEM and ARPR techniques. Identifying the crystal structure and obtaining the Raman spectrum of MnPS$_3$ flakes lay a solid foundation for follow-up research. The Heisenberg-type antiferromagnetic order in MnPS$_3$ is confirmed by DC magnetization measurements. Anisotropic behaviors of magnetic moments of the MnPS$_3$ crystal are discussed based on the MFA model. The confirmation of ambipolar conducting channels in an antiferromagnetic semiconductor opens an avenue for exploring fundamental correlated phenomena, such as spin/valleytronics coupled to an antiferromagnetic order.

METHODS

Crystal Synthesis. The MnPS$_3$ single crystals were prepared by a chemical vapor transport method. The stoichiometric mixture of Mn, P, and S powder was sealed in an evacuated quartz tube. Plate-like single crystals can be obtained *via* the vapor transport growth with a temperature gradient from 650 to 600 °C. The composition and structure of MnPS$_3$ single crystals were checked by X-ray diffraction and energy-dispersive X-ray spectrometry.

TEM Characterization. The TEM samples are prepared by direct transfer from scotch tape to 400-mesh copper grids after mechanical exfoliation. The SAED and EELS are carried out with a JEM 2010F (JEOL, Japan) under 200 kV, and the HRSTEM is performed with a JEM ARM 200CF (JEOL, Japan), equipped with a CEOS probe corrector and a cold field-emission gun, also at an acceleration voltage of 200 kV for its highest resolution. A low probe current (less than 75 pA) is chosen to reduce electron radiation, and a convergence semiangle of around 35 mrad and an inner acquisition semiangle of 79 mrad were used in the HAADF STEM. The HRSTEM image is filtered through the standard Wiener deconvolution to increase its signal-to-noise ratio for a better display. The zero-loss peak in the EELS data is aligned to exact 0 eV, and the Mn-$L_{2,3}$ edge spectrum goes through the power-law background subtraction after that.

EDLT Fabrication. Thin flakes of $MnPS_3$ are prepared by micromechanical exfoliation of a single bulk crystal. The thickness of $MnPS_3$ flakes is verified by atomic force microscopy. Then the flakes are transferred on the top of another prepared boron nitride flake. Electron-beam lithography is then applied to define Hall patterns on the $MnPS_3$ flakes followed by electron-beam evaporation and lift-off techniques to deposit contact metals in the defined Hall patterns. Finally, standard Hall devices with side-gate electrodes are fabricated. The contact metal electrodes consist of $Ti/Au/SiO_2$ (5 nm/60 nm/30 nm), and the side electrodes are not covered by SiO_2. The contact metal electrodes are covered by SiO_2 to isolate the electrodes from direct contact with the ionic liquid. The sizes of the side-gate electrodes are much larger (area ratio $>10^3$) than those of the $MnPS_3$ flakes. The large area ratio is designed to make sure that the voltage drop is effectively applied at the interface between $MnPS_3$ flakes and the ionic liquid instead of between the side-gate electrode and ionic liquid. Thanks to the thin electric layer ($\sim$1 nm) formed between the ionic liquid and graphene surface, an extremely strong electric field ($\sim 5 \times 10^9$ V/m) is generated to introduce an extremely high density of charge carriers to the samples ($\sim 5.23 \times 10^{13}$ V^{-1} cm^{-2}). The ionic liquid is N,N-diethy1-N-(2-methoxyethy1)-N-methylammonium bis-(trifluoromethylsulfony1)imide.

ASSOCIATED CONTENT

Ⓢ Supporting Information

The Supporting Information is available free of charge on the ACS Publications website at DOI: 10.1021/acsnano.7b05856.

> Elemental analysis of the $MnPS_3$ flake, anisotropic Raman peaks of a 10 nm thick $MnPS_3$ flake, assignment of $MnPS_3$ Raman modes and phonon frequencies, electronic transfer curves of $MnPS_3$ flakes with different thicknesses, and the instability of $MnPS_3$ flakes (PDF)

AUTHOR INFORMATION

Corresponding Author
*E-mail: phwang@ust.hk.

ORCID Ⓞ
Gen Long: 0000-0002-2004-5455
Ning Wang: 0000-0002-4902-5589

Present Address
⊥Department of Physics, University of Arkansas, Fayetteville, Arkansas 72701, United States

Notes
The authors declare no competing financial interest.

REFERENCES

(1) Lin, M.-W.; Zhuang, H. L.; Yan, J.; Ward, T. Z.; Puretzky, A. A.; Rouleau, C. M.; Gai, Z.; Liang, L.; Meunier, V.; Sumpter, B. G.; et al. Ultrathin Nanosheets of CrSiTe 3: A Semiconducting Two-Dimensional Ferromagnetic Material. *J. Mater. Chem. C* **2016**, *4*, 315−322.

(2) Tian, Y.; Gray, M. J.; Ji, H.; Cava, R.; Burch, K. S. Magneto-Elastic Coupling in A Potential Ferromagnetic 2D Atomic Crystal. *2D Mater.* **2016**, *3*, 025035.

(3) Nicolosi, V.; Chhowalla, M.; Kanatzidis, M. G.; Strano, M. S.; Coleman, J. N. Liquid Exfoliation of Layered Materials. *Science* **2013**, *340*, 1226419.

(4) Zhang, X.; Zhao, X.; Wu, D.; Jing, Y.; Zhou, Z. MnPSe3Monolayer: A Promising 2D Visible-Light Photohydrolytic Catalyst with High Carrier Mobility. *Adv. Sci.* **2016**, *3*, 1600062.

(5) Lee, J.-U.; Lee, S.; Ryoo, J. H.; Kang, S.; Kim, T. Y.; Kim, P.; Park, C.-H.; Park, J.-G.; Cheong, H. Ising-Type Magnetic Ordering in Atomically Thin FePS3. *Nano Lett.* **2016**, *16*, 7433−7438.

(6) Du, K.-z.; Wang, X.-z.; Liu, Y.; Hu, P.; Utama, M. I. B.; Gan, C. K.; Xiong, Q.; Kloc, C. Weak Van der Waals stacking, Wide-Range Band Gap, and Raman Study on Ultrathin Layers of Metal Phosphorus Trichalcogenides. *ACS Nano* **2016**, *10*, 1738−1743.

(7) Wang, X.; Du, K.; Liu, Y. Y. F.; Hu, P.; Zhang, J.; Zhang, Q.; Owen, M. H. S.; Lu, X.; Gan, C. K.; Sengupta, P. Raman Spectroscopy of Atomically Thin Two-Dimensional Magnetic Iron Phosphorus Trisulfide (FePS3) Crystals. *2D Mater.* **2016**, *3*, 031009.

(8) Sandilands, L.; Shen, J.; Chugunov, G.; Zhao, S.; Ono, S.; Ando, Y.; Burch, K. Stability of Exfoliated Bi$_2$Sr$_2$Dy$_x$ Ca$_{1−x}$Cu$_2$O$_{8+\delta}$ Studied by Raman Microscopy. *Phys. Rev. B: Condens. Matter Mater. Phys.* **2010**, *82*, 064503.

(9) de Jongh, L. J.; Miedema, A. R. Experiments on Simple Magnetic Model Systems. *Adv. Phys.* **1974**, *23*, 1−260.

(10) González-Herrero, H.; Gómez-Rodríguez, J. M.; Mallet, P.; Moaied, M.; Palacios, J. J.; Salgado, C.; Ugeda, M. M.; Veuillen, J.-Y.; Yndurain, F.; Brihuega, I. Atomic-Scale Control of Graphene Magnetism by Using Hydrogen Atoms. *Science* **2016**, *352*, 437−441.

(11) Nair, R.; Sepioni, M.; Tsai, I.-L.; Lehtinen, O.; Keinonen, J.; Krasheninnikov, A.; Thomson, T.; Geim, A.; Grigorieva, I. Spin-Half Paramagnetism in Graphene Induced by Point Defects. *Nat. Phys.* **2012**, *8*, 199−202.

(12) McCreary, K. M.; Swartz, A. G.; Han, W.; Fabian, J.; Kawakami, R. K. Magnetic Moment Formation in Graphene Detected by Scattering of Pure Spin Currents. *Phys. Rev. Lett.* **2012**, *109*, 186604.

(13) Červenka, J.; Katsnelson, M.; Flipse, C. Room-Temperature Ferromagnetism in Graphite Driven by Two-Dimensional Networks of Point Defects. *Nat. Phys.* **2009**, *5*, 840−844.

(14) Ugeda, M. M.; Brihuega, I.; Guinea, F.; Gómez-Rodríguez, J. M. Missing Atom as A Source of Carbon Magnetism. *Phys. Rev. Lett.* **2010**, *104*, 096804.

(15) Uchoa, B.; Kotov, V. N.; Peres, N.; Castro Neto, A. Localized Magnetic States in Graphene. *Phys. Rev. Lett.* **2008**, *101*, 026805.

(16) Joy, P.; Vasudevan, S. Magnetism in the Layered Transition-Metal Thiophosphates M PS$_3$ (M= Mn, Fe, and Ni). *Phys. Rev. B: Condens. Matter Mater. Phys.* **1992**, *46*, 5425.

(17) Mayorga-Martinez, C. C.; Sofer, Z. k.; Sedmidubský, D.; Huber, S. t. p. n.; Eng, A. Y. S.; Pumera, M. Layered Metal Thiophosphite Materials: Magnetic, Electrochemical, and Electronic Properties. *ACS Appl. Mater. Interfaces* **2017**, *9*, 12563−12573.

(18) Ressouche, E.; Loire, M.; Simonet, V.; Ballou, R.; Stunault, A.; Wildes, A. Magnetoelectric MnPS 3 as A Candidate for Ferrotoroidicity. *Phys. Rev. B: Condens. Matter Mater. Phys.* **2010**, *82*, 100408.

(19) Wolf, S.; Awschalom, D.; Buhrman, R.; Daughton, J.; Von Molnar, S.; Roukes, M.; Chtchelkanova, A. Y.; Treger, D. Spintronics:

A Spin-Based Electronics Vision for the Future. *Science* **2001**, *294*, 1488−1495.

(20) Žutić, I.; Fabian, J.; Das Sarma, S. Spintronics: Fundamentals and Applications. *Rev. Mod. Phys.* **2004**, *76*, 323.

(21) Bogani, L.; Wernsdorfer, W. Molecular Spintronics Using Single-Molecule Magnets. *Nat. Mater.* **2008**, *7*, 179−186.

(22) Awschalom, D. D.; Flatté, M. E. Challenges for Semiconductor Spintronics. *Nat. Phys.* **2007**, *3*, 153−159.

(23) Mai, C.; Barrette, A.; Yu, Y.; Semenov, Y. G.; Kim, K. W.; Cao, L.; Gundogdu, K. Many-Body Effects in Valleytronics: Direct Measurement of Valley Lifetimes in Single-Layer MoS_2. *Nano Lett.* **2014**, *14*, 202−206.

(24) Ezawa, M. Spin Valleytronics in Silicene: Quantum Spin Hall−Quantum Anomalous Hall Insulators and Single-Valley Semimetals. *Phys. Rev. B: Condens. Matter Mater. Phys.* **2013**, *87*, 155415.

(25) Nebel, C. E. Valleytronics: Electrons Dance in Diamond. *Nat. Mater.* **2013**, *12*, 690−691.

(26) Li, X.; Cao, T.; Niu, Q.; Shi, J.; Feng, J. Coupling the Valley Degree of Freedom to Antiferromagnetic Order. *Proc. Natl. Acad. Sci. U. S. A.* **2013**, *110*, 3738−3742.

(27) Long, G.; Xu, S.; Zhang, T.; Wu, Z.; Wong, W. K.; Han, T.; Lin, J.; Cai, Y.; Wang, N. Charge Density Wave Phase Transition on the Surface of Electrostatically Doped Multilayer Graphene. *Appl. Phys. Lett.* **2016**, *109*, 183107.

(28) Ouvrard, G.; Brec, R.; Rouxel, J. Structural Determination of Some MPS_3 Layered Phases (M= Mn, Fe, Co, Ni and Cd). *Mater. Res. Bull.* **1985**, *20*, 1181−1189.

(29) Frindt, R.; Yang, D.; Westreich, P. Exfoliated Single Molecular Layers of $Mn_{0.8}PS_3$ and $Cd_{0.8}PS_3$. *J. Mater. Res.* **2005**, *20*, 1107−1112.

(30) Long, G.; Xu, S.; Shen, J.; Hou, J.; Wu, Z.; Han, T.; Lin, J.; Wong, W. K.; Cai, Y.; Lortz, R.; et al. Type-Controlled Nanodevices Based on Encapsulated Few-Layer Black Phosphorus for Quantum Transport. *2D Mater.* **2016**, *3*, 031001.

(31) Long, G.; Maryenko, D.; Shen, J.; Xu, S.; Hou, J.; Wu, Z.; Wong, W. K.; Han, T.; Lin, J.; Cai, Y.; et al. Achieving Ultrahigh Carrier Mobility in Two-dimensional Hole Gas of Black Phosphorus. *Nano Lett.* **2016**, *16*, 7768−7773.

(32) Kurosawa, K.; Saito, S.; Yamaguchi, Y. Neutron Diffraction Study on $MnPS_3$ and $FePS_3$. *J. Phys. Soc. Jpn.* **1983**, *52*, 3919−3926.

(33) Liu, E.; Fu, Y.; Wang, Y.; Feng, Y.; Liu, H.; Wan, X.; Zhou, W.; Wang, B.; Shao, L.; Ho, C.-H.; et al. Integrated Digital Inverters Based on Two-Dimensional Anisotropic ReS_2 Field-Effect Transistors. *Nat. Commun.* **2015**, *6*, 6991.

(34) Kuo, C.-T.; Neumann, M.; Balamurugan, K.; Park, H. J.; Kang, S.; Shiu, H. W.; Kang, J. H.; Hong, B. H.; Han, M.; Noh, T. W.; et al. Exfoliation and Raman Spectroscopic Fingerprint of Few-Layer $NiPS_3$ Van der Waals Crystals. *Sci. Rep.* **2016**, *6*, 20904.

(35) Claassen, H. H.; Selig, H.; Shamir, J. Raman Apparatus Using Laser Excitation and Polarization Measurements. Rotational Spectrum of Fluorine. *Appl. Spectrosc.* **1969**, *23*, 8−12.

(36) Allemand, C. D. Depolarization Ratio Measurements in Raman Spectrometry. *Appl. Spectrosc.* **1970**, *24*, 348−353.

(37) Gonze, X.; Jollet, F.; Abreu Araujo, F.; Adams, D.; Amadon, B.; Applencourt, T.; Audouze, C.; Beuken, J.-M.; Bieder, J.; Bokhanchuk, A.; et al. Recent Developments in the ABINIT Software Package. *Comput. Phys. Commun.* **2016**, *205*, 106−131.

(38) Gonze, X.; Amadon, B.; Anglade, P.-M.; Beuken, J.-M.; Bottin, F.; Boulanger, P.; Bruneval, F.; Caliste, D.; Caracas, R.; Côté, M.; et al. ABINIT: First-Principles Approach to Material and Nanosystem Properties. *Comput. Phys. Commun.* **2009**, *180*, 2582−2615.

(39) Gonze, X. A Brief Introduction to the ABINIT Software Package. *Z. Kristallogr. - Cryst. Mater.* **2005**, *220*, 558−562.

(40) Gonze, X.; Beuken, J.-M.; Caracas, R.; Detraux, F.; Fuchs, M.; Rignanese, G.-M.; Sindic, L.; Verstraete, M.; Zerah, G.; Jollet, F.; et al. First-Principles Computation of Material Properties: the ABINIT Software Project. *Comput. Mater. Sci.* **2002**, *25*, 478−492.

(41) Bernasconi, M.; Marra, G.; Benedek, G.; Miglio, L.; Jouanne, M.; Julien, C.; Scagliotti, M.; Balkanski, M. Lattice Dynamics of Layered MPX_3 (M= Mn, Fe, Ni, Zn; X= S, Se) Compounds. *Phys. Rev. B: Condens. Matter Mater. Phys.* **1988**, *38*, 12089.

(42) Wu, J.; Mao, N.; Xie, L.; Xu, H.; Zhang, J. Identifying the Crystalline Orientation of Black Phosphorus Using Angle-Resolved Polarized Raman Spectroscopy. *Angew. Chem.* **2015**, *127*, 2396−2399.

(43) Chittari, B. L.; Park, Y.; Lee, D.; Han, M.; MacDonald, A. H.; Hwang, E.; Jung, J. Electronic and Magnetic Properties of Single-Layer MPX_3 Metal Phosphorous Trichalcogenides. *Phys. Rev. B: Condens. Matter Mater. Phys.* **2016**, *94*, 184428.

(44) Liu, J.; Li, X.-B.; Wang, D.; Lau, W.-M.; Peng, P.; Liu, L.-M. Diverse and Tunable Electronic Structures of Single-Layer Metal Phosphorus Trichalcogenides for Photocatalytic Water Splitting. *J. Chem. Phys.* **2014**, *140*, 054707.

(45) Saito, Y.; Nakamura, Y.; Bahramy, M. S.; Kohama, Y.; Ye, J.; Kasahara, Y.; Nakagawa, Y.; Onga, M.; Tokunaga, M.; Nojima, T.; et al. Superconductivity Protected by Spin-Valley Locking in Ion-Gated MoS_2. *Nat. Phys.* **2016**, *12*, 144−149.

(46) Grasso, V.; Silipigni, L. Low Dimensional Materials: The MPX_3 Family, Physical Features and Potential Future Applications. *Riv. Nuovo Cimento.* **2002**, *25*, 06.

(47) Brec, R.; Schleich, D.; Ouvrard, G.; Louisy, A.; Rouxel, J. Physical Properties of Lithium Intercalation Compounds of the Layered Transition-Metal Chalcogenophosphites. *Inorg. Chem.* **1979**, *18*, 1814−1818.

(48) Grasso, V.; Neri, F.; Santangelo, S.; Silipigni, L.; Piacentini, M. Electronic Conduction in the Layered Semiconductor $MnPS_3$. *J. Phys.: Condens. Matter* **1989**, *1*, 3337.

(49) Okuda, K.; Kurosawa, K.; Saito, S.; Honda, M.; Yu, Z.; Date, M. Magnetic Properties of Layered Compound $MnPS_3$. *J. Phys. Soc. Jpn.* **1986**, *55*, 4456−4463.

(50) Sales, B.; Wohlleben, D. Susceptibility of Interconfiguration-Fluctuation Compounds. *Phys. Rev. Lett.* **1975**, *35*, 1240.

(51) Hamaker, H.; Woolf, L.; MacKay, H.; Fisk, Z.; Maple, M. Coexistence of Superconductivity and Antiferromagnetic Order in $SmRh_4B_4$. *Solid State Commun.* **1979**, *32*, 289−294.

(52) Tan, H.; Verbeeck, J.; Abakumov, A.; Van Tendeloo, G. Oxidation State and Chemical Shift Investigation in Transition Metal Oxides by EELS. *Ultramicroscopy* **2012**, *116*, 24−33.

(53) Wildes, A.; Rønnow, H.; Roessli, B.; Harris, M.; Godfrey, K. Static and Dynamic Critical Properties of the Quasi-Two-Dimensional Antiferromagnet $MnPS_3$. *Phys. Rev. B: Condens. Matter Mater. Phys.* **2006**, *74*, 094422.

(54) Brec, R. Review on Structural and Chemical Properties of Transition Metal Phosphorous Trisulfides MPS_3. *Solid State Ionics* **1986**, *22*, 3−30.

(55) Goossens, D.; Wildes, A.; Ritter, C.; Hicks, T. Ordering and the Nature of the Spin flop Phase Transition in $MnPS_3$. *J. Phys.: Condens. Matter* **2000**, *12*, 1845.

(56) Goossens, D.; Hicks, T. The Magnetic Phase Diagram of $Mn_xZn_{(1-x)}PS_3$. *J. Phys.: Condens. Matter* **1998**, *10*, 7643.

(57) Wildes, A.; Roessli, B.; Lebech, B.; Godfrey, K. Spin Waves and the Critical Behaviour of the Magnetization in $MnPS_3$. *J. Phys.: Condens. Matter* **1998**, *10*, 6417.